

## Reference worldwide model for antineutrinos from reactors

Marica Baldoncini,<sup>1,2</sup> Ivan Callegari,<sup>3</sup> Giovanni Fiorentini,<sup>1,2,3</sup> Fabio Mantovani,<sup>1,2</sup> Barbara Ricci,<sup>1,2</sup>  
Virginia Strati,<sup>1,3</sup> and Gerti Xhixha<sup>3</sup>

<sup>1</sup>*Dipartimento di Fisica e Scienze della Terra, Università degli Studi di Ferrara, Via Saragat 1-44122, Ferrara, Italy*

<sup>2</sup>*INFN, Sezione di Ferrara, Via Saragat 1-44122, Ferrara, Italy*

<sup>3</sup>*Laboratori Nazionali di Legnaro, INFN, Viale dell'Università 2-35020 Legnaro, Italy*

(Received 24 November 2014; published 2 March 2015)

Antineutrinos produced at nuclear reactors constitute a severe source of background for the detection of geoneutrinos, which bring to the Earth's surface information about natural radioactivity in the whole planet. In this framework, we provide a reference worldwide model for antineutrinos from reactors, in view of reactors operational records yearly published by the International Atomic Energy Agency. We evaluate the expected signal from commercial reactors for ongoing (KamLAND and Borexino), planned (SNO+), and proposed (Juno, RENO-50, LENA, and Hanohano) experimental sites. Uncertainties related to reactor antineutrino production, propagation, and detection processes are estimated using a Monte Carlo-based approach, which provides an overall site-dependent uncertainty on the signal in the geoneutrino energy window on the order of 3%. We also implement the off-equilibrium correction to the reference reactor spectra associated with the long-lived isotopes, and we estimate a 2.4% increase of the unoscillated event rate in the geoneutrino energy window due to the storage of spent nuclear fuels in the cooling pools. We predict that the research reactors contribute to less than 0.2% to the commercial reactor signal in the investigated 14 sites. We perform a multitemporal analysis of the expected reactor signal over a time lapse of ten years using reactor operational records collected in a comprehensive database published at [www.fe.infn.it/antineutrino](http://www.fe.infn.it/antineutrino).

DOI: 10.1103/PhysRevD.91.065002

PACS numbers: 14.60.Pq, 13.15.+g

### I. INTRODUCTION

The existence of antineutrinos was first theorized in 1930 by Pauli, who attempted to explain the continuous electron energy distribution in beta decay as due to the emission of a third light, weakly interacting neutral particle. This prediction was confirmed in 1956 by Reines and Cowan in the Savannah River Experiment, in which inverse beta decay (IBD) reactions caused by electron antineutrinos from nuclear reactors were observed for the first time [1]. From then on, antineutrinos from nuclear reactors have played a crucial role in exploring neutrino physics, with respect to both the standard three-flavor neutrino oscillations and possible signatures of nonstandard neutrino interactions.

The observation of reactor antineutrino disappearance by the KamLAND (KL) experiment in 2005 [2] confirmed the neutrino oscillation as the mechanism behind the solar neutrino deficit identified in 2001 by the SNO experiment [3], opening the way to precise estimates of the oscillation parameters, as the recent determination of the nonzero value of  $\theta_{13}$ . Moreover, recent results from reactors pointed out an apparent 6% deficit of electron antineutrinos, referred to as the reactor antineutrino anomaly, which could be compatible with the existence of a fourth (sterile) neutrino [4].

Short-baseline and long-baseline reactor experiments, characterized, respectively, by a reactor-detector distance

small/long in comparison with a length scale on the order of 1 km, provided significant improvements in the accuracy of neutrino oscillation parameters [5–8]. Thanks to the remarkable progresses in the neutrino field over the last decades, the possibility of applying neutrino detection technologies for safeguard purposes is seriously under investigation [9]. In the neutrino puzzle, the feasibility of reactor antineutrino experiments at the medium baseline is currently being explored with the intent of probing neutrino oscillation parameters both at short and long wavelengths and of potentially investigating interference effects related to the mass hierarchy [10].

Concurrently, antineutrinos produced at nuclear reactors constitute a severe source of background for the detection of geoneutrinos, i.e., the electron antineutrinos produced in beta minus decays along the  $^{238}\text{U}$  and  $^{232}\text{Th}$  decay chains. As the energy spectrum of antineutrinos from nuclear reactors overlaps with the spectrum of geoneutrinos, a careful analysis of the expected reactor signal at specific experimental sites is mandatory to establish the sensitivity to geoneutrinos. Geoneutrinos are a real-time probe of the Earth's interior as their flux at the terrestrial surface depends on the amount and on the distribution of  $^{238}\text{U}$  and  $^{232}\text{Th}$  naturally present in the crust and in the mantle, which are thought to be the main reservoirs of these radioisotopes [11]. The first experimental evidence of geoneutrinos dates from 2005, when the KL collaboration

claimed the observation of four events associated with  $^{238}\text{U}$  and five with  $^{232}\text{Th}$  decay chains [12]. Recent results from the KL and Borexino (BX) experiments provided quantitative measurements of the geoneutrino signal ( $116_{-27}^{+28}$  observed events in a total live time of 2991 days for KL [8] and from  $14.3 \pm 4.4$  geoneutrino events in 1353 days for BX [13]), important for discriminating among different Earth compositional models.

The crustal contribution to the geoneutrino signal can be inferred from direct geochemical and geophysical surveys, while the mantle contribution is totally model dependent. A better discrimination among different compositional models of the bulk silicate Earth, referred to as “cosmochemical,” “geochemical,” and “geodynamical” [14], can be attained by combining the results from several sites [15]. Therefore, new measurements of geoneutrino fluxes are highly awaited from experiments entering operation, such as SNO+ [16], or proposed to the scientific community, such as Juno [17], RENO-50 [18], LENA [19], Hanohano [20], Homestake [21], and Baksan [22].

Electron antineutrinos are currently detected in liquid scintillation detectors via the IBD reaction on free protons

$$\bar{\nu}_e + p \rightarrow n + e^+, \quad (1)$$

which has an energy threshold of 1.806 MeV. As the antineutrino detection depends on several experimental parameters (e.g., the fiducial volume), expressing both geoneutrino and reactor antineutrino signals in terms of detector independent quantities allows the comparison of signals measured at different experiments and originating from different sources. Therefore, event rates are quoted in terrestrial neutrino units (TNUs) [11], corresponding to one event per  $10^{32}$  target protons per year, which are practical units as liquid scintillator mass is on the order of one kton ( $\sim 10^{32}$  free protons) and the exposure times are typically on the order of a few years.

Considering that the reactor antineutrino spectrum extends beyond the end point of that of the geoneutrinos, we observe a significant overlap between geoneutrino and reactor signals in the geoneutrino energy window (Fig. 1), where generally about 27% of the total reactor events are registered. The boundaries of this energy range, also specified as low-energy region (LER), are defined by the detection reaction threshold and by the maximum energy of emitted geoneutrinos, occurring in the  $^{214}\text{Bi}$  beta minus decay (3.272 MeV) [23]. The high-energy region (HER) extends from the upper edge of the LER to the end point of the reactor antineutrino spectrum. In this framework, modeling the predicted signal in the HER where only reactor events are expected is of decisive importance for understanding the reactor contribution in the LER. In particular, the ratio  $R_{\text{LER}}/G$  between the predicted reactor signal in the LER ( $R_{\text{LER}}$ ) and the expected geoneutrino signal ( $G$ ) can be considered as a figure of merit for

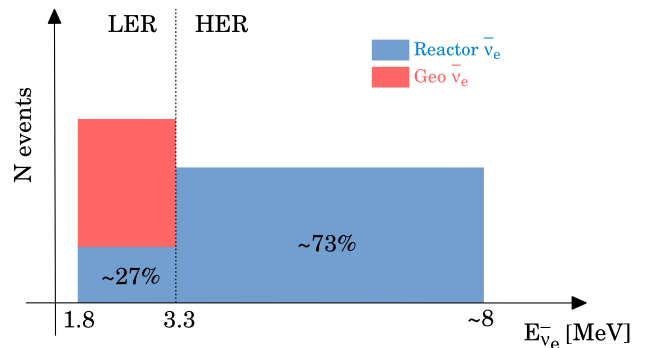


FIG. 1 (color online). A sketch of the expected reactor signal in the LER and in the HER. The reactor signal in the HER is crucial for modeling the reactor contribution in the LER and therefore for extracting information on geoneutrinos. The reactor contribution to the signal changes according to the different reactor operational conditions, while the geoneutrino component is time independent.

assessing the discrimination power on geoneutrinos at a specific location.

The focus of this paper is the calculation of the antineutrino signal from nuclear power plants, as fundamental background for geoneutrino measurements. Our work is structured as follows. In Sec. II, we present all the required ingredients for the calculation of the expected reactor signal, in which we distinguish the three distinctive antineutrino life stages, i.e., production, propagation, and detection. In Sec. III, we describe the Monte Carlo-based approach we adopt to estimate the global uncertainty on the reactor signal, together with the relative contributions related to each input quantity of the calculation. In Sec. IV, we present ten years (2003–2013) of reactor antineutrino signals at KL and BX, along with updated estimates of the expected reactor signals throughout the world, with a particular focus on ongoing and proposed experimental sites. In Sec. V, we summarize the main results of our work.

## II. INGREDIENTS IN THE CALCULATION OF THE REACTOR ANTINEUTRINO SIGNAL

The dominating background in geoneutrino studies is due to electron antineutrinos produced at nuclear power plants, which are the strongest man-made antineutrino sources. With an average energy released per fission of approximately 200 MeV and six antineutrinos produced along the beta minus decay chains of the neutron-rich unstable fission products,  $6 \times 10^{20} \bar{\nu}/\text{s}$  are emitted from a reactor having a thermal power of 3 GW. Evaluating the reactor antineutrino signal at a given location requires the knowledge of several ingredients, necessary for modeling the three reactor antineutrino life stages: production at reactor cores, propagation to the detector site, and detection in liquid scintillation detectors via the IBD reaction.

In our calculation, we consider all nonmovable operational reactors in the world used for commercial and research purposes. Hundreds of naval nuclear reactors with thermal power on the order of some hundreds of megawatts drive submarines, aircraft carriers, and icebreakers cruising around the world [24]. A discussion of the potential effect due to nuclear propelled vessels on neutrino measurements is provided in Ref. [25].

A comprehensive database dating back to 2003 has been compiled that contains the main features of each operational reactor core. The database is available at [www.fe.infn.it/antineutrino](http://www.fe.infn.it/antineutrino), and we plan to update it every year. The database structure is described in the Appendix.

### A. Spectra of antineutrinos produced at reactor cores

The operating principle of nuclear power reactors lies in the generation of heat by the neutron-induced fissions of U and Pu isotopes and by the subsequent decays of unstable fission fragments. In a typical reactor, more than 99.9% of antineutrinos above the IBD energy threshold are emitted in large Q-value beta decays of unstable daughter fragments that originated in the fission process of just four isotopes:  $^{235}\text{U}$ ,  $^{238}\text{U}$ ,  $^{239}\text{Pu}$ , and  $^{241}\text{Pu}$  [26]. Therefore, the antineutrino spectrum produced by a given reactor can be expressed, in units of  $\bar{\nu}/\text{MeV/fission}$ , as

$$\Lambda(E_{\bar{\nu}}) = \sum_{i=1}^4 f_i \lambda_i(E_{\bar{\nu}}), \quad (2)$$

where  $\lambda_i(E_{\bar{\nu}})$  and  $f_i$  are, respectively, the antineutrino emission spectrum normalized to one fission process and the fission fraction for the  $i$ th isotope, where  $i = ^{235}\text{U}$ ,  $^{238}\text{U}$ ,  $^{239}\text{Pu}$ , and  $^{241}\text{Pu}$ . In literature, the different fuel isotope contributions to the generated thermal power are expressed as fission fractions or as power fractions, which have to be considered as different physical quantities. The fission fraction  $f_i$  is defined as a relative fission yield, i.e., as the fraction of fissions produced by the  $i$ th isotope. This quantity is related to the reactor thermal power by the energy relation

$$P_{\text{th}} = R \langle Q \rangle = R \sum_{i=1}^4 f_i Q_i, \quad (3)$$

where  $R$  is total fission rate (number of fissions per unit time) and  $\langle Q \rangle$  is the average energy released per fission. The same energy relation can be expressed in terms of the power fractions  $p_i$ , corresponding to the fraction of the total thermal power produced by the fission of the  $i$  isotope,

$$P_{\text{th}} = p_i P_i = p_i R f_i Q_i, \quad (4)$$

where  $P_i$  is the thermal power generated by isotope  $i$ . Accordingly, the following relation between power fractions and fission fractions holds:

$$p_i = \frac{f_i Q_i}{\sum_{i=1}^4 f_i Q_i}. \quad (5)$$

During the power cycle of a nuclear reactor, the composition of the fuel changes as Pu isotopes are bred and U is consumed; thus, the power (fission) fractions are time-dependent quantities. Fuel isotope contributions also depend on the burnup technology adopted in the given reactor core as different core types are characterized by different fuel compositions, which in turn give rise to different isotope contributions to the total thermal power.

The nuclear reactor operation relies on the use of cooling and moderating materials, which should be as safe and as cheap as possible. Typical coolants include materials such as water or gas, which, due to their high thermal capacity, allow the collection and transfer of the energy released in the fission processes, while moderators are exploited to slow down the neutrons resulting from the fission processes to thermal energies in order to maintain the fission chain. Ordinary water is the most common moderator material; indeed, since hydrogen has a mass almost identical to that of the incident neutron, a single neutron-hydrogen collision can reduce the speed of the neutron substantially. However, due to the relatively high neutron capture cross section, reactors using light water as a moderator [such as pressurized water reactors (PWRs) and boiling water reactors (BWRs)] require the adoption of enriched uranium as nuclear fuel, with a typical enrichment level of  $^{235}\text{U}$  ranging from 2% to 5% [27]. Pressurized heavy water reactors (PHWRs) use heavy water as both a moderator and coolant; due to the smaller neutron capture cross section with respect to ordinary water, PHWRs can burn natural uranium. However, as the reactor design is flexible and allows the use of advanced fuel cycles, using slightly enriched uranium, recovered uranium, mixed oxide fuel (MOX), thorium fuels, and others [28] is possible. Gas cooled reactors (GCRs)<sup>1</sup> and light water graphite reactors (LWGRs) exploit graphite as a moderator, which allows the adoption of lower uranium enrichment levels, typically between 2.2% and 2.7% [29,30]. Few tens of reactors (mainly located in Europe) use MOX, which is a mix of more than one oxide of fissile material and usually consists of plutonium recovered from spent nuclear fuel, blended with natural uranium, reprocessed uranium, or depleted uranium. Generally, approximately 30% of the total power of these reactors comes from the MOX fuel, while the remaining 70% of the power is produced by standard fuel [31].

In our calculation of the emitted reactor antineutrino spectrum  $\Lambda(E_{\bar{\nu}})$ , we distinguish reactor classes according to the employed nuclear fuel. In Table I, we report typical

---

<sup>1</sup>Modern reactors using gas as a cooling material and graphite moderated are also referred to as advanced gas-cooled reactors (AGRs).

TABLE I.  $^{235}\text{U}$ ,  $^{238}\text{U}$ ,  $^{239}\text{Pu}$ , and  $^{241}\text{Pu}$  fission/power fractions for PWRs, BWRs, GCRs, LWGRs, PHWRs and for reactors burning MOX, taken from the references.

Reactor classes	Fractions	$^{235}\text{U}$	$^{238}\text{U}$	$^{239}\text{Pu}$	$^{241}\text{Pu}$	Reference
PWR	$f_i$	0.538	0.078	0.328	0.056	
		0.614	0.074	0.274	0.038	
		0.620	0.074	0.274	0.042	
		0.584	0.068	0.298	0.050	
		0.543	0.070	0.329	0.058	Mention <i>et al.</i> [33]
		0.607	0.074	0.277	0.042	
		0.603	0.076	0.276	0.045	
		0.606	0.074	0.277	0.043	
		0.557	0.076	0.313	0.054	
		0.606	0.074	0.274	0.046	
BWR	$f_i$	0.488	0.087	0.359	0.067	Abe <i>et al.</i> [7]
LWGR		0.580	0.074	0.292	0.054	
GCR		0.544	0.075	0.318	0.063	Djurcic <i>et al.</i> [26]
		0.577	0.074	0.292	0.057	
		0.590	0.070	0.290	0.050	Kopeikin <i>et al.</i> [34]
		0.570	0.078	0.295	0.057	Abe <i>et al.</i> [35]
		0.568	0.078	0.297	0.057	Eguchi <i>et al.</i> [36]
		0.563	0.079	0.301	0.057	Araki <i>et al.</i> [2]
		0.650	0.070	0.240	0.040	
		0.560	0.070	0.310	0.060	Kopeikin [37]
	$p_i$	0.480	0.070	0.370	0.080	
MOX		0.560	0.080	0.300	0.060	Bellini <i>et al.</i> [31]
PHWR		0.000	0.081	0.708	0.212	Bellini <i>et al.</i> [31]
	$p_i$	0.543	0.411	0.022	0.024	Bellini <i>et al.</i> [13]

fission/power fractions, together with the corresponding literature reference. PHWRs power fractions refer to reactors burning natural uranium [32]; therefore, we assign PWRs, BWRs, LWGRs, and GCRs to the same class of enriched uranium burning reactors.

The contribution to the reactor thermal power given by each fuel isotope depends on its specific fission fraction as well as on the energy released per fission  $Q_i$ , which is obtained by

$$Q_i = E_{\text{tot}}^i - \langle E_{\bar{\nu}} \rangle^i - \Delta E_{\beta\gamma}^i + E_{nc}^i, \quad (6)$$

where  $E_{\text{tot}}^i$  is the total energy produced in a fission process, starting from the moment the neutron that induces the process is absorbed until all of the unstable fission fragments have undergone beta decays;  $\langle E_{\bar{\nu}} \rangle^i$  is the mean energy carried away by antineutrinos produced in the beta decays of fission fragments;  $\Delta E_{\beta\gamma}^i$  is the energy of beta electrons and photons that, on average, does not contribute to the reactor energy during the operation of the core; and  $E_{nc}^i$  is the energy released in neutron capture (without fission) by the reactor core materials [38]. In Table II, we list the energies released per fission adopted in the calculation of the reactor antineutrino spectrum, which have been computed by Ma *et al.* [38] following the approach described in Eq. (6).

The distribution of the fission products of uranium or plutonium involves hundreds of nuclei, each of them

contributing to  $\lambda_i(E_{\bar{\nu}})$  through various beta decay chains. Thus, the total antineutrino spectrum is the result of the sum of thousands of beta branches, weighted by the branching ratio of each transition and by the fission yield of the parent nucleus. The two traditional ways for predicting the total antineutrino spectrum are the summation and the conversion methods. The summation procedure reconstructs the beta spectra using available nuclear databases as the sum of the branch-level beta spectra of all the daughter isotopes and then converts the beta spectra in the antineutrino spectra. The conversion technique relies on direct measurements of the beta spectra and exploits the energy conservation law between the two leptons involved in the beta minus decay,

$$E_e + E_{\bar{\nu}} = E_0, \quad (7)$$

where  $E_0$  is the endpoint of the beta transition.

TABLE II. Energy released per fission  $Q_i$  for  $^{235}\text{U}$ ,  $^{238}\text{U}$ ,  $^{239}\text{Pu}$ , and  $^{241}\text{Pu}$  taken from Ma *et al.* [38].

Fissile isotope	$Q_i$ (MeV)
$^{235}\text{U}$	$202.36 \pm 0.26$
$^{238}\text{U}$	$205.99 \pm 0.52$
$^{239}\text{Pu}$	$211.12 \pm 0.34$
$^{241}\text{Pu}$	$214.26 \pm 0.33$

In the 1980s, measurements of the total beta spectra of fissile isotopes were performed at the Laue-Langevin Institute (ILL) in Grenoble, where thin target foils of  $^{235}\text{U}$ ,  $^{239}\text{Pu}$ , and  $^{241}\text{Pu}$  were exposed to an intense thermal neutron flux and the beta spectra of the unstable fragments were measured [39–41]. These spectra act as benchmarks for the summation calculations and are direct inputs for the conversion method. As  $^{238}\text{U}$  undergoes fission when bombarded by fast neutrons, its beta spectrum could not be measured in the thermal flux of ILL. Recently, an experiment was performed at the neutron source Forschungs-Neutronenquelle Heinz Maier-Leibnitz in Garching to determine the cumulative antineutrino spectrum of the fission products of  $^{238}\text{U}$  [42].

In this work, we adopt as reference model the one published by Mueller *et al.* [43], in which the spectra of all four contributing isotopes are consistently given in terms of the exponential of a polynomial of order 5, as stated in Eq. (8). Mueller *et al.* [43] derive the  $^{235}\text{U}$ ,  $^{239}\text{Pu}$ , and  $^{241}\text{Pu}$  spectra based on a mixed approach that combines the accurate reference of the ILL electron spectra with the physical distribution of beta branches provided by the nuclear databases and calculates the  $^{238}\text{U}$  spectrum via a pure summation method:

$$\lambda_i(E_{\bar{\nu}}) = \exp \left( \sum_{p=1}^6 a_p^i E_{\bar{\nu}}^{p-1} \right). \quad (8)$$

In Table III, the coefficients of the polynomial function used in the parametrization of the reactor antineutrino spectrum generated by each fuel isotope are listed.

A reactor operational time profile is a required input for estimating the number of fissions occurring in a given time interval. The load factor  $LF$  is the percentage quantity expressing the effective working condition of a core in a specific period of the operating cycle and is defined as the ratio

$$LF = 100 \cdot \frac{EG}{REG}, \quad (9)$$

where  $EG$  is the net electrical energy produced during the reference period as measured at the unit outlet terminals, i.e., after subtracting the electrical energy taken by auxiliary units, while  $REG$  is the net electrical energy that

would have been supplied to the grid if the unit were operated continuously at the reference power unit during the whole reference period [44]. Load factor data are published by the International Atomic Energy Agency (IAEA) [44], both on a monthly timeline and as an annual average. In our calculation, we assume that published values of electrical load factors are equal to thermal load factors.

The spectrum of reactor antineutrinos emitted by a reactor core having a thermal power  $P_{\text{th}}$  and operating with a load factor  $LF$  can thus be evaluated according to Eq. (10):

$$S(E_{\bar{\nu}}) = P_{\text{th}} LF \sum_{i=1}^4 \frac{P_i}{Q_i} \lambda_i(E_{\bar{\nu}}). \quad (10)$$

## B. Propagation of antineutrinos during their movement to detector

The demonstration of the separate identity of muon and electron neutrinos [45], the discovery of the tauonic neutrino [46], and the measurement of the decay width of the Z boson at large electron-positron collider [47] endorsed the standard electroweak model (SEM) as the most reasonable theory describing neutrino physics, according to which neutrinos exist in three light (with masses smaller than  $1/2 M_Z$ ) flavors and separate lepton numbers for electron, muon, and tau flavors are conserved. Nevertheless, an observed deficit in the solar neutrino flux with respect to the prediction of the standard solar model started questioning the SEM, until the neutrino flavor change was definitely identified in 2001 by the SNO experiment [3] and subsequently the KL experiment provided clear evidence of the neutrino oscillatory nature [48].

At present, most experimental results on neutrino flavor oscillation agree with a three neutrino scenario, in which weak neutrino eigenstates, i.e., flavor eigenstates ( $\nu_e, \nu_\mu, \nu_\tau$ ), mix with the mass eigenstates ( $\nu_1, \nu_2, \nu_3$ ) via three mixing angles ( $\theta_{12}, \theta_{13}, \theta_{23}$ ) and a possible  $CP$ -violating phase  $\delta$ . Therefore, to establish the reactor antineutrino flux at a given site, it is necessary to consider the survival probability of the electron antineutrino, which can be expressed (assuming that antineutrinos propagate in vacuum) in terms of the mass-mixing oscillation parameters ( $\delta m^2, \theta_{12}, \theta_{13}$ ) as stated in Fiorentini *et al.* [49],

TABLE III. Coefficients of the polynomial of order 5 used as argument of the exponential function for the analytical expression of the antineutrino spectra for  $^{235}\text{U}$ ,  $^{238}\text{U}$ ,  $^{239}\text{Pu}$ , and  $^{241}\text{Pu}$ , taken from Mueller *et al.* [43].

Fissile isotope	$a_1$	$a_2$	$a_3$	$a_4$	$a_5$	$a_6$
$^{235}\text{U}$	3.217	-3.111	1.395	-3.690( $10^{-1}$ )	4.445( $10^{-2}$ )	-2.053( $10^{-3}$ )
$^{238}\text{U}$	4.833( $10^{-1}$ )	1.927( $10^{-1}$ )	-1.283( $10^{-1}$ )	-6.762( $10^{-3}$ )	2.233( $10^{-3}$ )	-1.536( $10^{-4}$ )
$^{239}\text{Pu}$	6.413	-7.432	3.535	-8.820( $10^{-1}$ )	1.025( $10^{-1}$ )	-4.550( $10^{-3}$ )
$^{241}\text{Pu}$	3.251	-3.204	1.428	-3.675( $10^{-1}$ )	4.254( $10^{-2}$ )	-1.896( $10^{-3}$ )

TABLE IV. The  $3\nu$  mass-mixing parameters entering the electron antineutrino survival probability equation, adapted from Capozzi *et al.* [50].

Oscillation parameter	Central value $\pm 1\sigma$ range
$\delta m^2$ (eV $^2$ )	$7.54 \pm 0.26$ (10 $^{-5}$ )
$\sin^2(\theta_{12})$	$3.08 \pm 0.17$ (10 $^{-1}$ )
$\sin^2(\theta_{13})$	$2.34 \pm 0.20$ (10 $^{-2}$ )

$$P_{ee}(E_{\bar{\nu}}, L) = \cos^4(\theta_{13}) \left( 1 - \sin^2(2\theta_{12}) \sin^2\left(\frac{\delta m^2 L}{4E_{\bar{\nu}}}\right) \right) + \sin^4(\theta_{13}), \quad (11)$$

where  $L$  and  $E_{\bar{\nu}}$  are the antineutrino path length and energy in natural units.<sup>2</sup>

In our calculation, we adopt the updated values on neutrino oscillation parameters, obtained by Capozzi *et al.* [50] from a global fit to data provided by different experiments.<sup>3</sup> The data combined analysis provides  $N\sigma$  curves of the  $3\nu$  oscillation parameters, the degree of linearity and symmetry of which is strictly related to the Gaussian nature of the probability distribution associated with that parameter. On the basis of Fig. 3 of Capozzi *et al.* [50], we assume  $(\delta m^2, \theta_{12}, \theta_{13})$  as described by Gaussian probability density functions (PDFs), and we adopt as central values and  $1\sigma$  uncertainties the values reported in Table IV, where, conservatively, the  $1\sigma$  value has been selected as the maximum between  $\sigma^+$  and  $\sigma^-$  for each parameter distribution.

We investigated the matter effect concerning the anti-neutrino propagation from the reactor to the experimental site by adopting the Earth density profile as published by Dziewonski and Anderson [53]. The matter effect on the signal varies according to the investigated experimental

<sup>2</sup>The three-flavor vacuum survival probability in principle depends on the difference between the squared masses  $\Delta m^2 = m_3^2 - (m_1^2 + m_2^2)/2$ , according to a relationship that is not invariant under a change of hierarchy (where  $\Delta m^2 > 0$  and  $\Delta m^2 < 0$  correspond, respectively, to the normal and inverted hierarchy scenarios). In any case, the  $\Delta m^2$  dependence of the survival probability is negligible for  $L \gg 50$  km [10]. Considering the quality of the inputs used for our calculation, the differences on the expected signal due to the use of two survival probabilities ( $\Delta m^2$  dependent and  $\Delta m^2$  not dependent) are negligible, which is true also in the cases of JUNO and RENO-50. The most general survival probability should be used for a spectral shape analysis, but it goes beyond the scope of this paper.

<sup>3</sup>During the refereeing process of the present work, new releases of oscillation parameters appeared by Forero *et al.* [51] and Gonzalez-Garcia *et al.* [52], affecting mainly the central values and the uncertainties on  $\sin^2(\theta_{12})$  and  $\sin^2(\theta_{13})$ . A check on the expected reactor signals shows central values variations within  $1\sigma$  reported in Table VII, together with a  $\sim 20\%$  decrease on the associated uncertainties. In this perspective, our estimations in Table VI and Table VII can be considered conservative.

site, giving a maximum contribution of 0.7% at Hawaii. In any case, it can be considered negligible at  $1\sigma$  level with respect to the overall uncertainties reported in Table VII.

With respect to the antineutrino path length, we evaluate  $L$  as the distance from the reactor to the experimental site using an ellipsoid as the geometrical shape of the Earth. We use  $a = 6378136.6$  m and  $b = 6356751.8$  m as the equatorial radius and polar radius, respectively [54].

### C. Detection of antineutrinos

The components presented in the last two sections allow the modeling of the expected (oscillated) reactor antineutrino flux at a given experimental site. To determine the predicted signal, it is necessary to account for the detection process via the IBD reaction on free protons. The IBD reaction effectiveness in antineutrino detection is the result of the relatively large reaction cross section (on the order of  $10^{-42}$  cm $^2$ ), the feasibility of building large detectors (as materials rich in free protons, such as water and hydrocarbons, are relatively cheap), and the possibility of reducing backgrounds, which is possible due to the correlation between the prompt positron annihilation signal and the delayed neutron capture signal [55]. In this work, we use for the parametrization of the IBD reaction cross section the expression given by Strumia and Vissani [56],

$$\sigma_{IBD}(E_{\bar{\nu}}) = 10^{-43} \text{ cm}^2 p_e E_e E_{\bar{\nu}}^{-0.07056 + 0.02018 \ln E_{\bar{\nu}} - 0.001953 \ln^3 E_{\bar{\nu}}}, \\ E_e = E_{\bar{\nu}} - \Delta, \quad p_e = \sqrt{E_e^2 - m_e^2}, \quad (12)$$

where  $E_e$  is the positron energy,  $\Delta = m_n - m_p \approx 1.293$  MeV,  $p_e$  is the positron momentum, and  $m_e = 0.511$  MeV is the positron mass. The final equation for the evaluation of the antineutrino signal from reactors is obtained considering the contribution at a given experimental site given by all operating reactors in the world, as stated in Eq. (13),

$$N_{\text{tot}} = \epsilon N_p \tau \sum_{i=1}^{N_{\text{reactor}}} \frac{P_{\text{th}}^i}{4\pi L_i^2} \langle LF_i \rangle \\ \times \int dE_{\bar{\nu}} \sum_{k=1}^4 \frac{p_k}{Q_k} \lambda_k(E_{\bar{\nu}}) P_{ee}(E_{\bar{\nu}}, L_i) \sigma_{IBD}(E_{\bar{\nu}}), \quad (13)$$

where  $\epsilon$  is the detector efficiency,  $N_p$  is the number of free target protons,  $\tau$  is the exposure time,  $\langle LF_i \rangle$  is the average load factor of the  $i$ th reactor over the given exposure time, and  $L_i$  is the reactor-detector distance. We evaluate the reactor antineutrino signal in TNUs and therefore assume a total number of free protons equal to  $N_p = 10^{32}$ , an acquisition time  $\tau = 3.15 \times 10^7$  s (1 yr), and a detector efficiency  $\epsilon = 1$ .

### III. ESTIMATION OF UNCERTAINTIES

The calculation of the reactor antineutrino signal at a given site requires the knowledge of many factors related to reactor physics, in terms of reactor operations and of nuclear physics describing the fission process, and to antineutrino physics, which involves both the oscillation and the detection mechanisms. Uncertainties with respect to input data contribute with different weights and in different ways to the uncertainty on the reactor signal. Thus, given the complexity of the model, we used a Monte Carlo-based approach to estimate the global uncertainty on the reactor signal, together with the relative contributions associated with each component of the calculation.

According to Ref. [57], for the evaluation of the uncertainty on the signal due to a specific input quantity  $X_i$ , we fix all the components to their central values and conduct a Monte Carlo sampling of  $X_i$  pseudorandom values according to their PDFs. With respect to the fission fractions, we assume as central values for the reactor class involving PWRs, BWRs, LWGRs, and GCRs the set reported by Bellini *et al.* [31]. In Table VI, we summarize the PDFs and the associated standard errors for the input quantities included in the propagation of the uncertainties, together with the reference from which each parameter has been extracted. Although moderate correlations among some signal input quantities (e.g., thermal power and fission fractions) have been investigated by Djurcic *et al.* [26], the analysis of their effects is out of the goal of this study as it would require punctual knowledge of input data (e.g., stage of burn up of the fuel and effective thermal power). In this framework, we treat each parameter as uncorrelated with other input quantities.

The signal uncertainties associated with each single input for the KL, BX, and SNO+ experiments (see Table VI) are obtained performing  $10^4$  calculations of the global signal produced by all operating reactors in the world in 2013 and using the reactor antineutrino spectrum provided by Mueller *et al.* [43].

With respect to the antineutrino oscillation parameters and the energy released per fission, the same  $X_i$  sampled value is used for all operating reactors for a given global signal calculation.

The fission fractions are extracted for the single cores for each of the  $10^4$  total reactor signal calculations at a given experimental site. The random sampling of the fission fractions allows us to take into account the lack of knowledge concerning the detailed fuel composition of each reactor as well as the unknown stage of burnup. The sampling is performed for PWRs, BWRs, and GCRs and for the 70% contribution given by standard fuels for reactors using the MOX technology. This is carried out by extracting with equal probability one of the 22 sets of fission fractions listed in Table I [constant probability mass function (PMF)]. For PHWRs and for the 30% MOX

component, the fixed values adopted are those presented by Bellini *et al.* [31] and Bellini *et al.* [13], listed in Table I. Although individual measurements of reactor thermal power can reach a subpercent level accuracy [26,27], the regulatory specifications for safe reactor operations for Japan and the United States require, at minimum, an accuracy of 2%. In our study, a conservative uncertainty value of 2% is adopted, including the error for thermal  $LF$ . We sample the thermal power of each core for every signal calculation.

The IBD cross section is extracted with a Monte Carlo sampling for each energy value at which the integrand of Eq. (12) is computed, in which the adopted energy bin is equal to 1 keV.

The global uncertainty of the reactor signal is evaluated by extracting simultaneously all the ingredients entering the uncertainty propagation procedure. This analysis is performed for 14 peculiar locations in the world, corresponding to sites hosting experiments that are currently ongoing or entering operation, as well as candidate sites for future neutrino experiments. Results are reported in Table VII, where the central values correspond to the medians and the errors are expressed as  $1\sigma$  uncertainties.

#### A. Effect of long-lived isotopes

During the operation of a nuclear reactor unstable fission, fragments are constantly being produced, with half-lives in a wide range, from fractions of seconds up to  $10^{18}$  years. The long-lived isotopes (LLIs) accumulate during the running of the reactor, and consequently there exist off-equilibrium effects in the antineutrino spectrum from an operating reactor. The  $^{235}\text{U}$ ,  $^{239}\text{Pu}$ , and  $^{241}\text{Pu}$  antineutrino reference spectra entering the calculation of the total reactor spectrum are determined from the beta spectra measured after an exposure time to thermal neutrons of 12 h ( $^{235}\text{U}$ ) [39], 1.5 days ( $^{239}\text{Pu}$ ) [40], and 1.8 days ( $^{241}\text{Pu}$ ) [41], which implies that long-lived fission fragments have not yet reached equilibrium. Among unstable fission products of energy in the region  $E_{\bar{\nu}}^{\max} > 1.806 \text{ MeV}$ , the most important LLIs having half-lives longer than 10 h contribute only in the LER (see Table V), as the amplitude of the positive deviation from the reference spectra becomes negligible above 3.5 MeV [43]. The list of LLIs includes the spent nuclear fuels (SNFs), i.e.,  $^{106}\text{Ru}$ ,  $^{144}\text{Ce}$ , and  $^{90}\text{Sr}$ , having  $\tau_{1/2} \sim \text{yr}$ . As the off-equilibrium effects associated with the LLIs affect the antineutrino signal in the LER, understanding the LLIs' contribution is a relevant issue in the geoneutrino framework.

We adopt the off-equilibrium corrections to the reference spectra reported in Table VII of Mueller *et al.* [43] in order to estimate the systematic uncertainty on the antineutrino signal due to the accumulation of LLIs during the running of the reactor. As the operational run of a reactor usually lasts one year, signal values reported in Table VII include the 300 days off-equilibrium correction to the reference

TABLE V. LLIs, responsible of the off-equilibrium contribution to the reactor antineutrino spectrum during the reactor operating period, together with the SNFs (in the last three rows), which contribute also after the shut down of the reactor.  $\tau_{1/2}^P$ ,  $\tau_{1/2}^D$ ,  $E_{\bar{\nu}}^{\max P}$ , and  $E_{\bar{\nu}}^{\max D}$  are the half-lives and the maximum energy of the emitted antineutrino of the parent (P) and daughter (D) nucleus, respectively [58].  $Y_{235}$  and  $Y_{239}$  are, respectively, the daughter cumulative specific yields in percentage per fission event of  $^{235}\text{U}$  and  $^{239}\text{Pu}$ , except for the case of  $^{93}\text{Y}$  and  $^{97}\text{Zr}$ , which refer to the parent nuclides [37].

P	$\tau_{1/2}^P$	$E_{\bar{\nu}}^{\max P}$ (MeV)	D	$\tau_{1/2}^D$	$E_{\bar{\nu}}^{\max D}$ (MeV)	$Y_{235}$ (%)	$Y_{239}$ (%)
$^{93}\text{Y}$	10.18 h	2.895	$^{93}\text{Zr}$	$1.61 \times 10^6$ yr	0.091	6.35	3.79
$^{97}\text{Zr}$	16.75 h	1.916	$^{97}\text{Nb}$	72.1 m	1.277	5.92	5.27
$^{112}\text{Pd}$	21.03 h	0.27	$^{112}\text{Ag}$	3.13 h	3.956	0.013	0.13
$^{131m}\text{Te}$	33.25 h	/	$^{131}\text{Te}$	25.0 m	2.085	0.09	0.20
$^{132}\text{Te}$	3.204 d	0.24	$^{132}\text{I}$	2.295 h	2.141	4.31	5.39
$^{140}\text{Ba}$	12.753 d	1.02	$^{140}\text{La}$	1.679 d	3.762	6.22	5.36
$^{144}\text{Ce}$	284.9 d	0.319	$^{144}\text{Pr}$	17.28 m	2.998	4.58	3.11
$^{106}\text{Ru}$	371.8 d	0.039	$^{106}\text{Rh}$	30.07 s	3.541	0.30	3.24
$^{90}\text{Sr}$	28.79 yr	0.546	$^{90}\text{Y}$	64.0 h	2.280	0.27	0.10

$^{235}\text{U}$ ,  $^{239}\text{Pu}$ , and  $^{241}\text{Pu}$  spectra published by Mueller *et al.* [43]. After a time lapse on the order of one month with respect to the end of a reactor operating cycle, the SNF that has been pulled out from the reactor contributes to approximately 0.6% of the IBD unoscillated event rate in the full-energy region (FER) (see Fig. 6 of Bin *et al.* [59]). Each reactor is generally subject to a scheduled preventive maintenance on a yearly basis during which one-third of the burned fuel is typically transferred to the water pool located near the reactor core for cooling and shielding. As the exhausted fuel storage time can be as long as ten years, the presence of the SNFs in the water pools can affect the reactor signal predictions, especially in the LER. We estimate an average SNF half-life weighting the individual half-lives of the SNF species for the relative yields and fission fractions associated with each fissioning isotope, as stated in the equation

$$\tau_{1/2}^{\text{SNF}} = \sum_{i=^{144}\text{Ce}, ^{106}\text{Ru}, ^{90}\text{Sr}} k_i \tau_{1/2}^i, \\ k_i = \sum_{l=^{235}\text{U}, ^{239}\text{Pu}} f_l \bar{Y}_l^i, \quad (14)$$

where  $\tau_{1/2}^i$  is the half-life of the  $i$ th SNF species,  $f_l$  is the fission fraction (normalized to unity) for the  $l$ th fissioning isotope, and  $\bar{Y}_l^i$  is the production yield, with the normalization constraint  $\sum_l \bar{Y}_l^i = 1$ . Following this approach, we estimate a SNF global half-life of

$$\tau_{1/2}^{\text{SNF}} = 1.9 \text{ yr}. \quad (15)$$

The enhancement of the unoscillated IBD event rate due to the SNFs in the FER  $\Delta N_{\text{IBD}}^{\text{SNF}}$  can be determined for a storage time  $T$  (expressed in units of years) according to Eq. (16),

TABLE VI. Uncertainty on the reactor signal in the FER for the long-baseline experiments KL, BX, and SNO+ due to the uncertainties on single inputs. Results are obtained by applying a Monte Carlo sampling of the input quantities according to the corresponding PDF.

Input quantity	Symbol	PDF	1 $\sigma$ uncertainty on input (%)	Reference for input	1 $\sigma$ uncertainty on signal in the FER (%)		
					BX	KL	SNO+
$\bar{\nu}$ oscillation	$\delta m^2$	Gaussian	3.4	Capozzi <i>et al.</i> [50]	<0.1	0.9	<0.1
	$\sin^2(\theta_{12})$	Gaussian	5.5		+2.4/-2.2	+2.1/-2.0	+2.4/-2.2
	$\sin^2(\theta_{13})$	Gaussian	8.5		0.4	0.4	0.4
Energy released per fission	$Q_k$	$Q_{^{235}\text{U}}$	0.1	Ma <i>et al.</i> [38]	<0.1	<0.1	<0.1
	$Q_{^{238}\text{U}}$		0.3				
	$Q_{^{239}\text{Pu}}$		0.2				
	$Q_{^{241}\text{Pu}}$		0.2				
Fuel composition	$f_k$	$f_{^{235}\text{U}}$	Constant PMF	Table I	0.1	0.5	<0.1
		$f_{^{238}\text{U}}$					
		$f_{^{239}\text{Pu}}$					
		$f_{^{241}\text{Pu}}$					
Thermal Power	$P_{th}$	Gaussian	2	Djurcic <i>et al.</i> [26]	0.2	0.9	0.3
IBD cross section	$\sigma_{\text{IBD}}(E_{\bar{\nu}})$	Gaussian	0.4	Strumia and Vissani [56]	<0.1	<0.1	<0.1

TABLE VII. Predicted antineutrino signals (in TNU) from nuclear power plants in the FER ( $R_{FER}$ ) and in the LER ( $R_{LER}$ ) obtained with 2013 reactor operational data, together with the expected geoneutrino signals (G) and  $R_{LER}/G$  ratios at current and proposed neutrino experimental sites. Antineutrino signals in the FER and in the LER include the off-equilibrium contribution due to the accumulation of the LLIs during the running of the reactor. For the KL experiment, we report also the values obtained using 2006 reactor operating records. For the Juno experiment, we predict the 2020 reactor signals, considering as operating with a 80% annual average load factor the Yangjiang (17.4 GW) and Taishan (18.4 GW) nuclear power stations, which are actually under construction.

Site	Experiment	Coordinates	G (TNU)	$R_{FER}$ (TNU)	$R_{LER}$ (TNU)	$R_{LER}/G$
Gran Sasso (IT) <sup>a</sup>	Borexino	42.45 N, 13.57 E <sup>b</sup>	$40.3^{+7.3}_{-5.8}$	$83.3^{+2.0}_{-1.9}$	$22.2^{+0.6}_{-0.6}$	0.6
Sudbury (CA)	SNO+	46.47 N, 81.20 W <sup>b</sup>	$45.4^{+7.5}_{-6.3}$	$190.9^{+4.6}_{-4.2}$	$47.8^{+1.7}_{-1.4}$	1.1
Kamioka (JP)	KamLAND	36.43 N, 137.31 E <sup>b</sup>	$31.5^{+4.9}_{-4.1}$	$65.3^{+1.7}_{-1.6}$	$18.3^{+0.6}_{-1.0}$	0.6
DongKeng (CH)	Juno	22.12 N, 112.52 E <sup>d</sup>	$39.7^{+6.5}_{-5.2}$	$95.3^{+2.6}_{-2.4}$	$26.0^{+2.2}_{-2.3}$	0.7
				$625.9^{+14.5}_{-13.2}$ <sup>c</sup>	$168.5^{+5.7}_{-6.3}$ <sup>c</sup>	5.3 <sup>c</sup>
				$1566^{+111}_{-100}$ <sup>e</sup>	$354.5^{+44.5}_{-40.6}$ <sup>e</sup>	8.9 <sup>e</sup>
GuemSeong (SK)	RENO-50	35.05 N, 126.70 E <sup>d</sup>	$38.3^{+6.1}_{-4.9}$	$1128^{+75}_{-67}$	$178.4^{+20.8}_{-19.6}$	4.7
Hawaii (US)	Hanohano	19.72 N, 156.32 W <sup>b</sup>	$12.0^{+0.7}_{-0.6}$	$3.4^{+0.1}_{-0.1}$	$0.9^{+0.02}_{-0.02}$	0.1
Pyhäsalmi (FI)	LENA	63.66 N, 26.05 E <sup>b</sup>	$45.5^{+6.9}_{-5.9}$	$66.1^{+1.6}_{-1.5}$	$17.0^{+0.5}_{-0.4}$	0.4
Boulby (UK)	LENA	54.55 N, 0.82 W <sup>b</sup>	$39.2^{+6.3}_{-4.9}$	$1234^{+35}_{-35}$	$240.6^{+11.5}_{-11.9}$	6.1
Canfranc (SP)	LENA	42.70 N, 0.52 W <sup>b</sup>	$40.0^{+6.4}_{-5.1}$	$247.4^{+5.8}_{-5.5}$	$70.3^{+1.6}_{-1.7}$	1.8
Fréjus (FR)	LENA	45.13 N, 6.68 E <sup>b</sup>	$42.8^{+7.6}_{-6.4}$	$546.7^{+11.9}_{-10.5}$	$126.0^{+5.4}_{-5.1}$	2.9
Slănic (RO)	LENA	45.23 N, 25.94 E <sup>b</sup>	$45.1^{+7.8}_{-6.3}$	$109.2^{+2.7}_{-2.5}$	$29.6^{+0.7}_{-0.7}$	0.7
Sieroszowice (PL)	LENA	51.55 N, 16.03 E <sup>b</sup>	$43.4^{+7.0}_{-5.6}$	$153.3^{+3.8}_{-3.6}$	$41.4^{+1.1}_{-1.1}$	1.0
Homestake (US)	/	44.35 N, 103.75 W <sup>b</sup>	$48.7^{+8.3}_{-6.9}$	$30.4^{+0.7}_{-0.7}$	$8.0^{+0.2}_{-0.2}$	0.2
Baksan (RU)	/	43.20 N, 42.72 E <sup>b</sup>	$47.2^{+7.7}_{-6.4}$	$36.6^{+0.9}_{-0.8}$	$9.6^{+0.3}_{-0.3}$	0.2

<sup>a</sup>IT: Italy, JP: Japan, CA: Canada, CH: China, SK: South Korea, US: United States of America, FI: Finland, UK: United Kingdom, SP: Spain, FR: France, RO: Romania, PL: Poland, and RU: Russia.

<sup>b</sup>Huang *et al.* [15]

<sup>c</sup>2006 reactor operational data.

<sup>d</sup>Ciuffoli *et al.* [60]

<sup>e</sup>2013 reactor operational data plus Yangjiang (17.4 GW) and Taishan (18.4 GW) nuclear power stations operating with a 80% average annual load factor.

$$\Delta N_{IBD}^{SNF} = \sum_{n=0}^T 0.2 \cdot \exp\left(-\frac{n}{\tau_{SNF}}\right), \quad (16)$$

where we assume that every year a SNF mass equal to one-third of the reactor mass, decaying with a mean lifetime  $\tau^{SNF} = \tau_{1/2}^{SNF} / \ln(2)$ , is transferred to the cooling pools.

With the hypothesis of a ten-year storage time of SNFs, corresponding to the convergence of the series in Eq. (16), we estimate a 2.4% increase of the unoscillated IBD event rate in the LER, in agreement with Refs. [8] and [12]. This potentially critical systematic uncertainty in geoneutrino measurements is not included in Table VII.

## B. Research reactors

The research reactor (RR) class embraces a wide range of civil nuclear reactors that are generally not employed for power generation but are mainly used as neutron sources, as well as for innovative nuclear energy researches and for teaching/training purposes. Among the major applications of the produced neutron beams are the nondestructive tests of materials, neutron scattering experiments, and

the production of radioisotopes both for medical and industrial uses.

According to the 2013 IAEA data published in Ref. [61], there are 247 operational RR in the world, accounting for a total thermal power of 2.2 GW, to be compared with the 1160 GW global thermal power generated by the 441 operational commercial reactors. Half of the RR thermal power is generated by only eight reactors having an individual thermal power between 100 and 250 MW. We calculate the expected reactor signal in the 14 experimental sites listed in Table VII, originating from the 40 RRs that account for the 90% of the thermal power considering an average 80% annual load factor. The effect of this contribution is in any case smaller than 0.2%, which can be considered as an upper limit enhancement of the commercial reactor signal.

## IV. RESULTS AND COMMENTS

In Table VI, we report the results of our estimate of the uncertainties on the reactor signal due to the  $1\sigma$  errors associated with single inputs. For the three operative

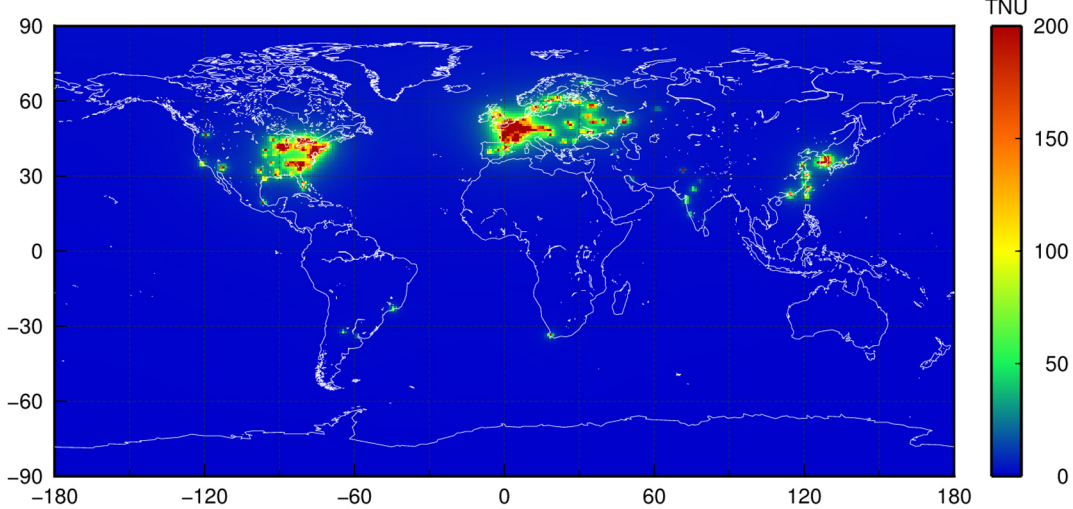


FIG. 2 (color online). Map of the worldwide predicted antineutrino signals from nuclear power plants in the LER, expressed in TNUs. The map has a spatial resolution of  $1^\circ \times 1^\circ$ , and it is produced with 2013 operational data on nuclear power plants.

long-baseline experiments, the major effect is attributed to  $\sin^2(\theta_{12})$ , which generates an uncertainty on the signal of approximately 2.2% at  $1\sigma$  level.

The impact on the signal uncertainty due to the uncertainties on reactors thermal power and on the fission fractions is highly site dependent. It emerges as a combined effect of the different reactor distances from the experimental sites and of the number and class of close-by reactors.

In 2013, approximately 60% of the signal predicted at KL was almost equally shared between just two Japanese reactor cores (Ohi stations 3 and 4), which are located 180 km far away from the Kamioka mine. The same signal percentage is produced at BX by approximately 60 reactors located within a radius of 1000 km, in which each core contributes to less than 3% of the signal. With respect to SNO+, 20 cores situated within a 500 km radius from the experimental site provide approximately 60% of the signal, each core contributing to 6% of the signal at maximum (see Fig. 5). As a consequence, the uncertainty on reactors thermal power generates at KL an uncertainty on the signal three times higher than what estimated for BX and SNO+, on the order of 1%.

Fission fractions give rise to a few tenths of percent  $1\sigma$  uncertainty on the reactor signal. The effect of fission fractions at KL is five times larger with respect to that estimated at BX; this behavior reproduces the one already observed for the thermal power and is also related to the fact that reactors giving the highest contributions to the signal belong to the same reactor class. On the other hand, SNO+ is almost insensitive to fission fractions variability, since the signal is dominated by the Canadian PHWRs, for which a fixed single set of power fractions is currently available.

In this work, we present also a worldwide map (with a  $1^\circ \times 1^\circ$  spatial resolution) of expected reactor signals in the LER expressed in TNUs, produced using 2013 operational reactor data (see Fig. 2). This map provides evidence

regarding the sites demonstrating the best discrimination power on geoneutrino measurements.

A particular focus is dedicated to sites hosting ongoing neutrino experiments (KL and BX), experiments entering operation (SNO+), and candidate sites for future experiments (Juno, RENO-50, Hanohano, LENA, Homestake, and Baksan). For these specific locations, we evaluate the expected reactor signal both in the FER ( $R_{FER}$ ) and in the LER ( $R_{LER}$ ) and the predicted geoneutrino signal  $G$  on the base of the reference Earth model published by Huang *et al.* [15]. We also evaluate the ratio  $R_{LER}/G$ , which can be considered as a figure of merit for assessing the sensitivity to geoneutrinos at a given site (see Table VII).

The reactor signals  $R_{FER}$  and  $R_{LER}$  are determined as median values of the signal distributions obtained from the Monte Carlo calculation. For each site, the signals are computed  $10^4$  times using the Mueller *et al.* [43] analytical parametrization of the reactor spectrum, including the 300 days off-equilibrium correction due to the LLIs, and simultaneously extracting, according to the corresponding PDF, all the inputs entering the uncertainty propagation procedure as described in Sec. III. For the long-baseline experiments, signal errors are evaluated as  $1\sigma$  uncertainties and are estimated to be on the order of 3% and 4% for the signal in the FER and in the LER, respectively. Ratios  $R_{LER}/G$  between predicted geoneutrino and reactor signals in the LER (calculated using 2013 reactor operational features) show the high discrimination power on geoneutrinos achievable at Hawaii ( $R_{LER}/G = 0.1$ ), Homestake, and Baksan ( $R_{LER}/G = 0.2$ ). In 2013, a relatively high sensitivity to geoneutrinos was attainable at Kamioka ( $R_{LER}/G = 0.6$ ) thanks to the protracted shutdown of the Japanese reactors after the Fukushima accident, in comparison with the much lower geoneutrino discrimination power of 2006 ( $R_{LER}/G = 5.4$ ) when the Japanese power industry was fully operational. Moreover, Juno appears to be a good

TABLE VIII. Reactor signals (without the LLIs contribution) in the FER and in the LER obtained with the analytical parametrization of the reactor spectra from Huber [62], Huber and Schwetz [63], Vogel and Engel [64], and Mueller *et al.* [43] for the BX, KL, and SNO+ experiments. Since in Refs. [63] and [62] there is no analytical expression for the  $^{238}\text{U}$  antineutrino spectrum, the one reported in Mueller *et al.* [43] is used in these two cases.

Reactor spectra model	$R_{\text{FER}}$ (TNU)			$R_{\text{LER}}$ (TNU)		
	BX	KL	SNO+	BX	KL	SNO+
Mueller <i>et al.</i> [43]	$83.2^{+2.0}_{-1.8}$	$65.3^{+1.7}_{-1.6}$	$190.2^{+4.8}_{-4.3}$	$22.1^{+0.6}_{-0.5}$	$18.3^{+0.6}_{-1.0}$	$47.2^{+1.7}_{-1.4}$
Huber [62] + $^{238}\text{U}$ Mueller <i>et al.</i> [43]	$83.9^{+2.0}_{-1.8}$	$65.9^{+1.7}_{-1.6}$	$192.0^{+4.9}_{-4.3}$	$22.0^{+0.6}_{-0.5}$	$18.3^{+0.6}_{-1.0}$	$47.1^{+1.7}_{-1.4}$
Huber and Schwetz [63] + $^{238}\text{U}$ Mueller <i>et al.</i> [43]	$81.2^{+2.0}_{-1.8}$	$63.7^{+1.6}_{-1.5}$	$185.5^{+4.7}_{-4.1}$	$21.7^{+0.6}_{-0.5}$	$18.0^{+0.6}_{-1.0}$	$46.3^{+1.7}_{-1.4}$
Vogel and Engel [64]	$81.6^{+2.0}_{-1.8}$	$63.9^{+1.6}_{-1.6}$	$187.1^{+4.7}_{-4.2}$	$21.6^{+0.5}_{-0.6}$	$17.9^{+0.6}_{-1.0}$	$46.0^{+1.7}_{-1.4}$

candidate site for geoneutrino measurements according to 2013 reactors operating status. If the experiment construction is achieved before the completion of the Yangjiang (17.4 GW) and Taishan (18.4 GW) nuclear power plants, the 20 kton detector will reach a 10% accuracy on geoneutrinos in approximately 105 days (assuming a  $\text{C}_{17}\text{H}_{28}$  liquid scintillator composition, a 100% detection efficiency, and that the geoneutrino background is due only to reactor antineutrinos). In contrast, we predict that the ratio  $R_{\text{LER}}/G$  dramatically increases from 0.7 to 8.9 if we consider both Chinese power stations to operate with an annual average load factor of 80%.

To estimate the variability in the expected reactor signal due to different reactor spectra, we calculate the predicted signals at KL, BX, and SNO+ using three alternative parametrizations of the antineutrino spectra, i.e., the ones

published by Huber [62], Huber and Schwetz [63], and Vogel and Engel [64] (see Table VIII). There is no expression for the  $^{238}\text{U}$  spectrum in Refs. [63] and [62], as these parametrizations are based on the conversion of ILL beta spectra. Therefore, for these two sets of spectra, the adopted functional expression for the  $^{238}\text{U}$  antineutrino spectrum is provided by Mueller *et al.* [43]. Median signal values are shown in Table VIII, together with the  $1\sigma$  uncertainties evaluated via Monte Carlo sampling. The maximum signal spread associated with the employment of different analytical functions as a phenomenological parametrization of the reactor antineutrino spectrum is of the same order as the global uncertainty on the signal resulting from the combined effect of all the other input quantities. Therefore, the reactor antineutrino spectrum emerges as the most critical component in the signal calculation.

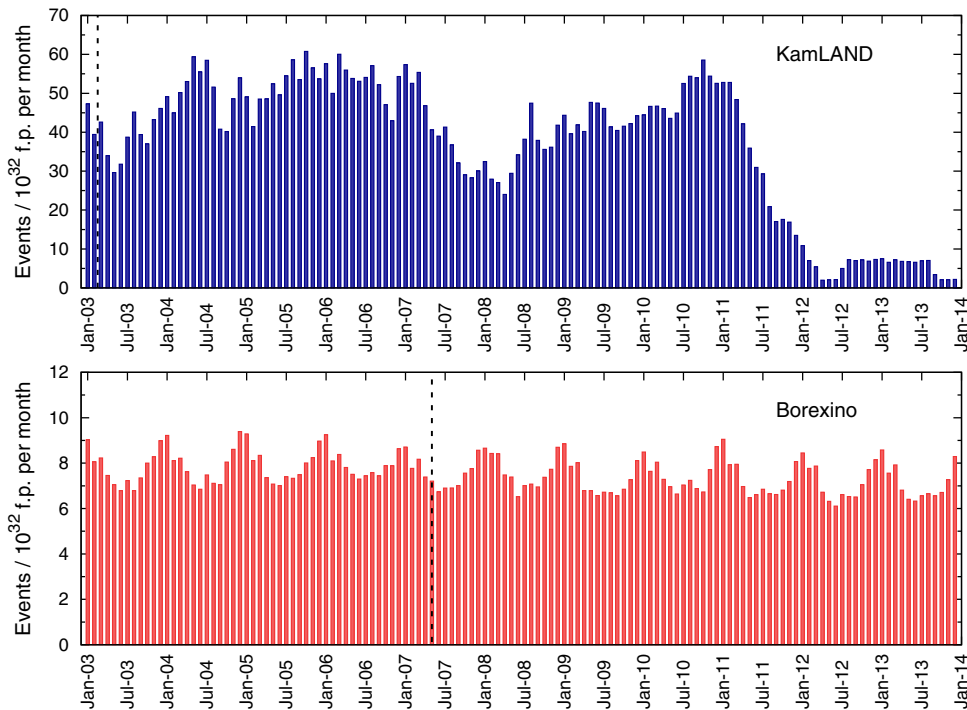


FIG. 3 (color online). Reactor signals in the FER for the KL experiment (blue panel) and for the BX experiment (red panel), calculated from January 2003 to December 2013 on a monthly timeline. The vertical dashed lines indicate the data taking start of the experiments (March 2003 for KL and May 2007 for BX).

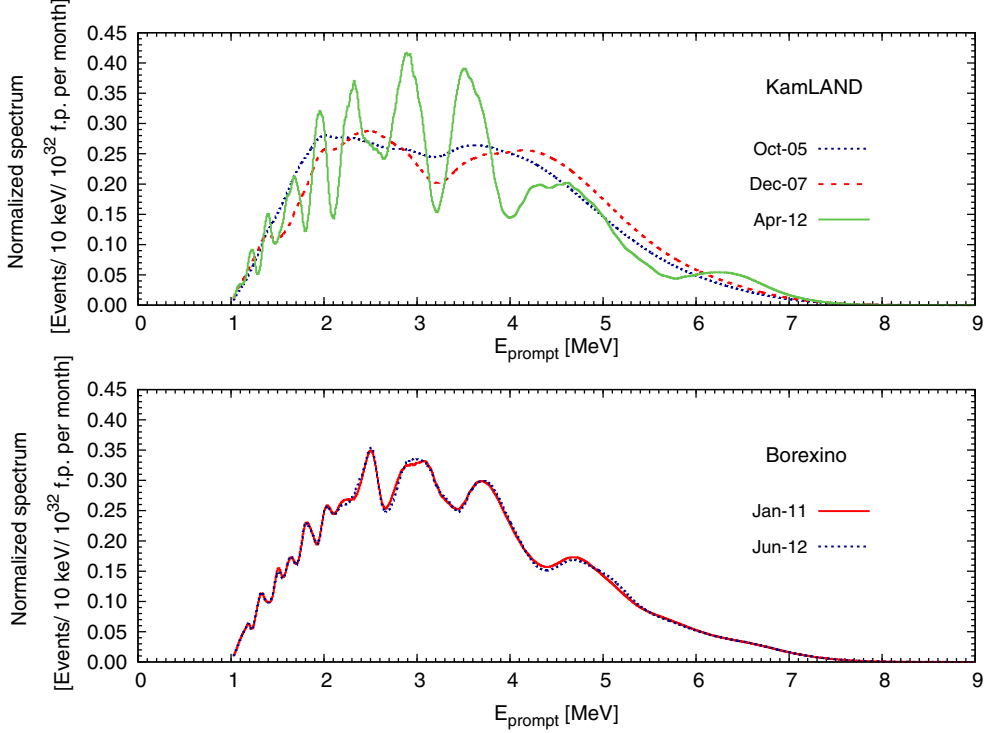


FIG. 4 (color online). Reactor antineutrino spectra above the IBD threshold for the KL experiment (upper panel) and for the BX experiment (lower panel) calculated over different data-taking periods. KL spectra are evaluated over three peculiar time intervals, corresponding to a maximum, an average, and a minimum expected reactor signal (October 2005, December 2007, and April 2012, respectively). BX spectra are calculated in correspondence to a winter and a summer seasonal signal variation (January 2011 and June 2012). All the spectra are normalized to the signal corresponding to the specific month.

We present a time profile of the expected reactor antineutrino signals at KL and BX over a period of 10 years on a monthly timeline, from 2003, when the KL detector entered operation, to 2013 (see Fig. 3).

The BX time profile exhibits a seasonal variation, suggesting that the periodic signal shape could be possibly implemented in the event analysis. The highest and lowest reactor signals occur, respectively, in correspondence with the cold and warm seasons, being that the electricity demand is typically higher during the winter. In connection to this, it can be noticed that refueling and maintenance for nuclear units are typically performed in the spring and fall seasons, when demand for electricity is generally lower. In Ref. [13], the antineutrino event analysis on a 1353 days data-taking period shows a good agreement with our prediction, although the seasonal variation has not been studied.

The KL signal time profile is instead highly affected by the operating conditions of the Japanese reactors. The shutdown of nuclear power plants concomitant to strong earthquakes in Japan is therefore manifestly visible as a pronounced decrease in the evaluated reactor signal. In particular, there is clear evidence of the protected shutdown of the Kashiwazaki-Kariwa and Hamaoka nuclear power plants subsequent to the Chuetsu earthquake in July 2007 and of the protected shutdown of the entire Japanese

nuclear reactor industry following the Fukushima nuclear accident in March 2011.

The different signal time profiles for the two experiments reflect also in different reactor antineutrino spectra (see Fig. 4). As understood from the contribution on the signal uncertainty given by the reactor thermal power and fission

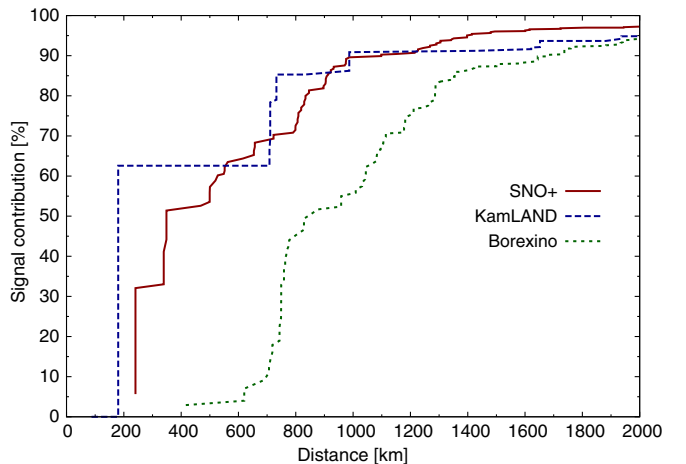


FIG. 5 (color online). Cumulative percentage contribution to the total expected reactor signal as a function of the distance of the reactors from the experimental site for KL, BX, and SNO+. Data refer to the 2013 reactor operational period.

fraction uncertainties (see Table VI), the antineutrino spectrum at BX is relatively insensitive to different operational conditions of individual nuclear power plants, as there are no close-by reactors dominating the antineutrino flux. Conversely, detailed information on the operating status of the near reactors emerges as a fundamental piece of knowledge for modeling the reactor spectrum at KL.

The distribution of the cumulative percentage contribution to the total reactor signal as a function of the distance of the reactors from the experimental site (see Fig. 5) yields a hint of the level of criticality associated with the knowledge of the

operational parameters of reactors. The KL distance profile has a steplike function shape: the first discontinuity is observed at 180 km where the signals coming from units 3 and 4 of the Ohi nuclear power plant sum up and provide approximately 60% of the total reactor signal. The second and third discontinuities in the KL distribution (85% and 90% of the total signal, respectively) occur for a reactor-detector distance of 730 km (corresponding to the contribution given by all operating Japanese reactors and by the South Korean reactors located on the East coast) and 990 km (summing up the contribution of the Hanbit power plant,

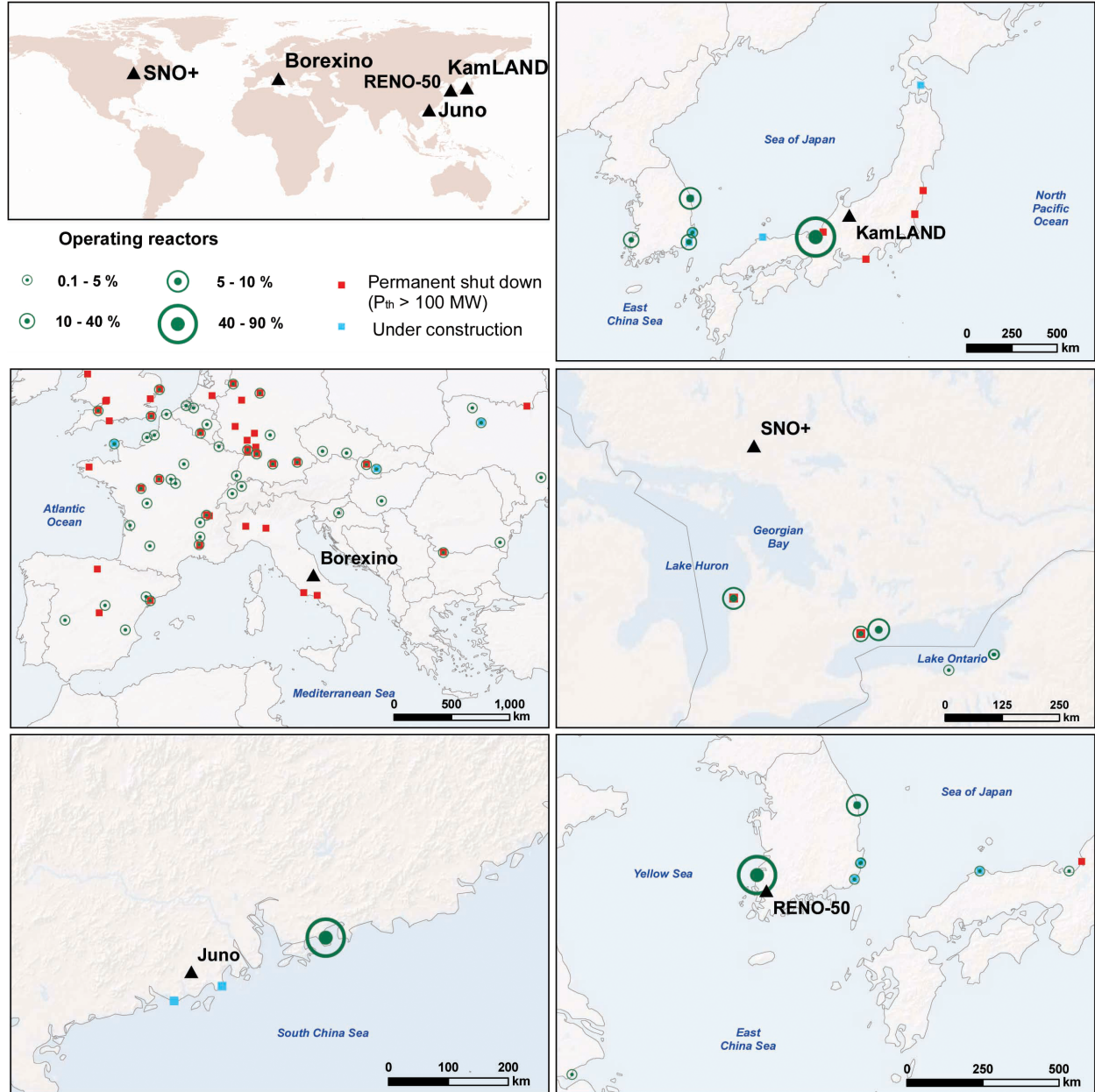


FIG. 6 (color online). Location map of the percentage contributions to the reactor signal given by the close-by reactors for the three long-baseline experiments KL, BX, and SNO+ and for the proposed medium-baseline experiments Juno and RENO-50. The map is produced with 2013 reactor operational data.

located in West South Korea). The BX distance profile is smoother compared to that of KL as the reactor signal is gradually spread out over the European countries. With respect to BX, the closest power station is at a distance of 415 km (Slovenia), which contributes the major fraction of the reactor signal, i.e., approximately 3%. With respect to the SNO+ experiment, the distribution is dominated at short distance by the Canadian Bruce power station, corresponding to the first step in the distance profile at 240 km (32% of the signal). The second step is associated with the Pickering and Darlington power plants and occurs at a site-reactor distance of 350 km (51% of the signal). For a site-reactor distance greater than 500 km, the profile levels out due to the contributions given by the more distant power stations located in the United States.

The percentage contributions to the signal given by the relatively close reactors at long-baseline experiments (KL, BX and SNO+) and at proposed medium-baseline experiments (Juno and RENO-50) are displayed on a location map (see Fig. 6). In addition to the contributions of operating power plants in 2013, nuclear stations under construction are displayed.

## V. CONCLUSIONS

One of the primary goals of the current and proposed reactor neutrino experiments is to investigate the neutrino properties at different wavelengths according to different reactor-detector baselines. While shedding light on the oscillatory neutrino nature, neutrino experiments also provide insight into the Earth's interior via the detection of geoneutrinos. In this framework, nuclear power plants emerge as the most severe background sources as approximately 27% of the reactor event rate is recorded in the geoneutrino energy window. The main results of this work are as follows:

- (i) We evaluated the expected antineutrino signal from nonmovable reactors for 14 peculiar locations in the world, estimating its uncertainties in view of reactors operational information yearly published by the Power Reactor Information System (PRIS) of the IAEA. A comprehensive database concerning nuclear power plants operational status is published at [www.fe.infn.it/antineutrino](http://www.fe.infn.it/antineutrino), and we plan to update it every year. We evaluated the expected antineutrino signal from reactors and from the Earth for 14 peculiar locations in the world, corresponding to sites hosting experiments that are currently ongoing or entering operation, as well as candidate sites for future neutrino experiments.
- (ii) The Monte Carlo method applied for the propagation of (uncorrelated) uncertainties on reactor signals associated with the input quantities provided an overall uncertainty for the long-baseline experiments of approximately 3% in the FER and of approximately 4% in the LER, for a fixed analytical expression of the

reactor spectrum. The reactor signal uncertainty is dominated by  $\sin^2(\theta_{12})$ , which solely provides an uncertainty of approximately 2.2% in the FER for KL, BX, and SNO+.

- (iii) We performed a comparison of the reactor signals obtained using different reactor spectra, which revealed that the uncertainty related to the antineutrino spectrum is as critical as the combined uncertainty of the other input quantities appearing in the signal calculation.
- (iv) We discussed the effect of the systematic enhancement of the reactor antineutrino spectrum due both to the accumulation of the LLIs during the operation of a reactor and to the storage of the SNFs in the cooling pools. We estimate a 2.4% increase of the unoscillated IBD event rate in the LER due to the SNFs that potentially can be a critical systematic uncertainty in geoneutrino measurements.
- (v) We estimated that the RRs producing a total thermal power of 2.2 GW contribute less than 0.2% to the commercial reactor signal in the investigated 14 sites.
- (vi) We presented a multitemporal analysis of the expected reactor signal at BX and KL over a time lapse of ten years. With respect to BX, a periodic seasonal signal variation associated with the lower fall-spring electricity demand is recognized: expected reactor signals are relatively insensitive to the operational conditions of single cores, since there are no close-by reactors dominating the antineutrino flux. Conversely, the KL signal time profile is governed by the Japanese nuclear industry operational status, which makes the shutdown of nuclear power plants concomitant to strong earthquakes manifestly visible.

## ACKNOWLEDGMENTS

The authors would like to thank C. Rott for the useful information on RENO-50 and J. Mandula for the valuable help in the compilation of the nuclear reactors database. We are also grateful to J. Esposito, T. Lasserre, D. Lhuillier, L. Ludhova, Th. A. Mueller, and S. Zavatarelli for the useful comments. We appreciate geological insights from R. L. Rudnick, W. F. McDonough, and Y. Huang. We wish to thank the two anonymous reviewers for their detailed and thoughtful reviews. This work was partially supported by the Istituto Nazionale di Fisica Nucleare through the ITALIAN RADactivity project and by the University of Ferrara through the research initiative “Fondo di Ateneo per la Ricerca scientifica FAR 2014.”

## APPENDIX THE DATABASE OF THE OPERATING COMMERCIAL REACTORS

The database of the operating commercial reactors has been compiled starting in 2003 up to now on a yearly basis and updated using the operational information yearly

published by the PRIS of the IAEA (<http://www.iaea.org/pris/home.aspx>). The nuclear power plant database contains 19 columns, structured as follows (for a given year of operation):

- (i) core country acronym;
- (ii) core name;
- (iii) core location (latitude and longitude in decimal degrees);
- (iv) core type;
- (v) use of MOX (1 for yes, 0 for no);

- (vi) thermal power  $P_{\text{th}}$  [MW];
- (vii) 12 columns listing the load factor for each month, expressed in percentage.

Latitude and longitude of core locations are taken from the World Nuclear Association Database (<http://world-nuclear.org/NuclearDatabase/Default.aspx?id=27232>). Core country acronyms, core name, core type, thermal and electrical power, and load factors are defined and published in the PRIS annual publication entitled [44] “Operating Experience with Nuclear Power Stations in Member States.”

- 
- [1] C. L. Cowan, F. Reines, F. B. Harrison, H. W. Kruse, and A. D. McGuire, *Science* **124**, 103 (1956).
  - [2] T. Araki *et al.* (KamLAND Collaboration), *Phys. Rev. Lett.* **94**, 081801 (2005).
  - [3] Q. R. Ahmad *et al.* (SNO Collaboration), *Phys. Rev. Lett.* **87**, 071301 (2001).
  - [4] K. N. Abazajian *et al.*, [arXiv:1204.5379](https://arxiv.org/abs/1204.5379).
  - [5] F. P. An *et al.* (Daya Bay Collaboration), *Chin. Phys. C* **37**, 011001 (2013).
  - [6] J. K. Ahn *et al.* (RENO Collaboration), *Phys. Rev. Lett.* **108**, 191802 (2012).
  - [7] Y. Abe *et al.* (Double Chooz Collaboration), *Phys. Rev. Lett.* **108**, 131801 (2012).
  - [8] A. Gando *et al.* (KamLAND Collaboration), *Phys. Rev. D* **88**, 033001 (2013).
  - [9] T. Lasserre, M. Fechner, G. Mention, R. Reboulleau, M. Cribier, A. Letourneau, and D. Lhuillier, [arXiv: 1011.3850](https://arxiv.org/abs/1011.3850).
  - [10] F. Capozzi, E. Lisi, and A. Marrone, *Phys. Rev. D* **89**, 013001 (2014).
  - [11] G. Fiorentini, M. Lissia, and F. Mantovani, *Phys. Rep.* **453**, 117 (2007).
  - [12] T. Araki *et al.* (KamLAND Collaboration), *Nature (London)* **436**, 499 (2005).
  - [13] G. Bellini *et al.* (Borexino Collaboration), *Phys. Lett. B* **722**, 295 (2013).
  - [14] O. Šrámek, W. F. McDonough, E. S. Kite, V. Lekić, S. T. Dye, and S. Zhong, *Earth Planet. Sci. Lett.* **361**, 356 (2013).
  - [15] Y. Huang, V. Chubakov, F. Mantovani, R. L. Rudnick, and W. F. McDonough, *Geochemistry, Geophysics, Geosystems* **14**, 2003 (2013).
  - [16] J. Maneira and T. S. Collaboration, *J. Phys. Conf. Ser.* **447**, 012065 (2013).
  - [17] Y.-F. Li, *Int. J. Mod. Phys. Conf. Ser.* **31**, 1460300 (2014).
  - [18] S. B. Kim, International Workshop on RENO-50 toward Neutrino Mass Hierarchy, Seoul National University, Korea, 2013..
  - [19] M. Wurm *et al.*, *Astropart. Phys.* **35**, 685 (2012).
  - [20] B. Cicenas and N. Solomey, *Phys. Procedia* **37**, 1324 (2012).
  - [21] N. Tolich, Y.-D. Chan, C. A. Currat, B. K. Fujikawa, R. Henning, K. T. Lesko, A. W. P. Poon, M. P. Decowski, J. Wang, and K. Tolich, *Earth Moon Planets* **99**, 229 (2007).
  - [22] G. V. Domogatsky, V. I. Kopeikin, L. A. Mikaelyan, and V. V. Sinev, *Physics At. Nucl.* **68**, 69 (2005).
  - [23] G. Fiorentini, A. Ianni, G. Korga, M. Lissia, F. Mantovani, L. Miramonti, L. Oberauer, M. Obolensky, O. Smirnov, and Y. Suvorov, *Phys. Rev. C* **81**, 034602 (2010).
  - [24] S. E. Hirdaris, Y. F. Cheng, P. Shallcross, J. Bonafoux, D. Carlson, B. Prince, and G. A. Sarris, *Ocean Eng.* **79**, 101 (2014).
  - [25] J. Detwiler, G. Gratta, N. Tolich, and Y. Uchida, *Phys. Rev. Lett.* **89**, 191802 (2002).
  - [26] Z. Djurcic, J. A. Detwiler, A. Piepke, V. R. Foster, L. Miller, and G. Gratta, *J. Phys. G* **36**, 045002 (2009).
  - [27] C. Bemporad, G. Gratta, and P. Vogel, *Rev. Mod. Phys.* **74**, 297 (2002).
  - [28] B. Rouben, CANDU Fuel-Management Course, Atomic Energy of Canada Limited, Montreal, Canada (1999).
  - [29] P. Podvig, Science and global security: the technical basis for arms control and environmental policy initiatives **19**, 46 (2011).
  - [30] E. Nonbøl, Report No. NKS-RAK-2(96)TR-C2, 1996.
  - [31] G. Bellini *et al.* (Borexino Collaboration), *Phys. Lett. B* **687**, 299 (2010).
  - [32] E. Cristoph, D. G. Hurst, A. M. Marko, D. K. Myers, F. C. Boyd, B. Ullyett, G. C. Hanna, T. A. Eastwood, J. C. D. Milton, H. K. Rae, M. F. Duret, C. E. Ells, R. E. Bain, R. E. Green, R. G. Hart, and J. A. L. Robertson, *Canada Enters the Nuclear Age: A Technical History of Atomic Energy of Canada Limited* (McGill-Queen's University Press, Canada, 1997).
  - [33] G. Mention, M. Fechner, T. Lasserre, T. A. Mueller, D. Lhuillier, M. Cribier, and A. Letourneau, *Phys. Rev. D* **83**, 073006 (2011).
  - [34] V. I. Kopeikin, L. A. Mikaelyan, and V. V. Sinev, *Phys. At. Nucl.* **67**, 1892 (2004).
  - [35] S. Abe *et al.* (KamLAND Collaboration), *Phys. Rev. Lett.* **100**, 221803 (2008).
  - [36] K. Eguchi *et al.* (KamLAND Collaboration), *Phys. Rev. Lett.* **90**, 021802 (2003).
  - [37] V. I. Kopeikin, *Phys. At. Nucl.* **75**, 143 (2012).

- [38] X. B. Ma, W. L. Zhong, L. Z. Wang, Y. X. Chen, and J. Cao, *Phys. Rev. C* **88**, 014605 (2013).
- [39] K. Schreckenbach, G. Colvin, W. Gelletly, and F. Von Feilitzsch, *Phys. Lett. B* **160**, 325 (1985).
- [40] F. von Feilitzsch, A. A. Hahn, and K. Schreckenbach, *Phys. Lett. B* **118**, 162 (1982).
- [41] A. A. Hahn, K. Schreckenbach, W. Gelletly, F. von Feilitzsch, G. Colvin, and B. Krusche, *Phys. Lett. B* **218**, 365 (1989).
- [42] N. Haag, A. Gütlein, M. Hofmann, L. Oberauer, W. Potzel, K. Schreckenbach, and F. Wagner, *Phys. Rev. Lett.* **112**, 122501 (2014).
- [43] T. A. Mueller, D. Lhuillier, M. Fallot, A. Letourneau, S. Cormon, M. Fechner, L. Giot, T. Lasserre, J. Martino, G. Mention, A. Porta, and F. Yermia, *Phys. Rev. C* **83**, 054615 (2011).
- [44] J. Mandula, Nuclear Power Engeneering Section, International Atomic Energy Agency, IAEA-PRIS database, Report No. IAEA-STI/PUB/1671, 2014.
- [45] G. Danby, J.-M. Gaillard, K. Goulianos, L. M. Lederman, N. Mistry, M. Schwartz, and J. Steinberger, *Phys. Rev. Lett.* **9**, 36 (1962).
- [46] K. Kodama *et al.*, *Phys. Lett. B* **504**, 218 (2001).
- [47] D. E. Groom *et al.* (Particle Data Group), *Eur. Phys. J. C* **15** (2000) 1.
- [48] A. Gando *et al.* (KamLAND Collaboration), *Phys Rev D* **83**, 052002 (2011).
- [49] G. Fiorentini, G. L. Fogli, E. Lisi, F. Mantovani, and A. M. Rotunno, *Phys Rev D* **86**, 033004 (2012).
- [50] F. Capozzi, G. Fogli, E. Lisi, A. Marrone, D. Montanino, and A. Palazzo, *Phys. Rev. D* **89**, 093018 (2014).
- [51] D. V. Forero, M. Tortola, and J. W. F. Valle, *Phys. Rev. D* **90** (2014).
- [52] M. C. Gonzalez-Garcia, M. Maltoni, and T. Schwetz, *J. High Energy Phys.* **11** (2014) 052.
- [53] A. M. Dziewonski and D. L. Anderson, *Phys. Earth Planet. Inter.* **25**, 297 (1981).
- [54] International Earth Rotation and Reference Systems Service (IERS), IERS Technical Note No. 32 (2003).
- [55] G. R. Jocher, D. A. Bondy, B. M. Dobbs, S. T. Dye, J. A. Georges, III, J. G. Learned, C. L. Mulliss, and S. Usman, *Phys. Rep.* **527**, 131 (2013).
- [56] A. Strumia and F. Vissani, *Phys. Lett. B* **564**, 42 (2003).
- [57] Joint Committee for Guides in Metrology, JCGM 101 (2008).
- [58] <http://www.nndc.bnl.gov/nudat2/>.
- [59] Z. Bin, R. Xi-Chao, N. Yang-Bo, Z. Zu-Ying, A. Feng-Peng, and C. Jun, *Chin. Phys. C* **36**, 1 (2012).
- [60] E. Ciuffoli, J. Evslin, Z. Wang, C. Yang, X. Zhang, and W. Zhong, *Phys. Rev. D* **89**, 073006 (2014).
- [61] <http://nucleus.iaea.org/RRDB/RR/ReactorSearch.aspx?rf=1>.
- [62] P. Huber, *Phys. Rev. C* **84**, 024617 (2011).
- [63] P. Huber and T. Schwetz, *Phys. Rev. D* **70**, 053011 (2004).
- [64] P. Vogel and J. Engel, *Phys. Rev. D* **39**, 3378 (1989).